







Article

# Structural Characterization of Dissolved Organic Matter in Permafrost Peatland Lakes

Diogo Folhas <sup>1,2,3,\*</sup>, Armando C. Duarte <sup>2</sup> , Martin Pilote <sup>3,4</sup>, Warwick F. Vincent <sup>3,5</sup> , Pedro Freitas <sup>3,6</sup> , Gonalo Vieira <sup>6</sup>, Artur M. S. Silva <sup>7</sup> , Regina M. B. O. Duarte <sup>2</sup>  and Joo Canrio <sup>1</sup> 

<sup>1</sup> Centro de Qumica Estrutural, Instituto Superior Tcnico, Universidade de Lisboa, 1049-001 Lisboa, Portugal; joao.canario@tecnico.ulisboa.pt

<sup>2</sup> Department of Chemistry & CESAM, University of Aveiro, 3810-193 Aveiro, Portugal; aduarte@ua.pt (A.C.D.); regina.duarte@ua.pt (R.M.B.O.D.)

<sup>3</sup> Centre d'tudes nordiques (CEN), Universit Laval, Quebec City, QC G1V 0A6, Canada; martin.pilote@canada.ca (M.P.); warwick.vincent@bio.ulaval.ca (W.F.V.); pedro-freitas@campus.ul.pt (P.F.)

<sup>4</sup> Environment and Climate Change Canada, Aquatic Contaminants Research Division, Montreal, QC H2Y 2E7, Canada

<sup>5</sup> Dpartement de biologie, Universit Laval, Quebec City, QC G1V 0A6, Canada

<sup>6</sup> Centro de Estudos Geogrficos, Instituto de Geografia e Ordenamento do Territrio, Universidade de Lisboa, 1600-276 Lisboa, Portugal; vieira@edu.ulisboa.pt

<sup>7</sup> Department of Chemistry & QOPNA and LAQV-REQUIMTE, University of Aveiro, 3810-193 Aveiro, Portugal; artur.silva@ua.pt

\* Correspondence: diogo.folhas@tecnico.ulisboa.pt

Received: 14 October 2020; Accepted: 29 October 2020; Published: 31 October 2020



**Abstract:** Thermokarst lakes result from the thawing of ice-rich permafrost and are widespread across northern landscapes. These waters are strong emitters of methane, especially in permafrost peatland regions, where they are stained black by high concentrations of dissolved organic matter (DOM). In the present study, we aimed to structurally characterize the DOM from a set of peatland thermokarst lakes that are known to be intense sites of microbial decomposition and methane emission. Samples were collected at different depths from three thermokarst lakes in the Sasapimakwananisikw (SAS) River valley near the eastern Hudson Bay community of Kuujjuarapik–Whapmagoostui (Nunavik, Canada). Samples were analyzed by spectrofluorometry, Fourier-transform infrared spectroscopy (FTIR), nuclear magnetic resonance spectroscopy (NMR), and elemental analysis. Fluorescence analyses indicated considerable amounts of autochthonous DOM in the surface waters of one of SAS 1A, indicating a strong bioavailability of labile DOM, and consequently a greater methanogenic potential. The three lakes differed in their chemical composition and diversity, suggesting various DOM transformations phenomena. The usefulness of complementary analytical approaches to characterize the complex mixture of DOM in permafrost peatland waters cannot be overlooked, representing a first step towards greater comprehension of the organic geochemical properties of these permafrost-derived systems.

**Keywords:** permafrost; thermokarst; peatlands; subarctic; DOM; carbon cycle

## 1. Introduction

Perennially frozen ground or permafrost, defined as soil or rock that remains at least two years at or below 0 °C, underlies up to one-quarter of Northern Hemisphere lands [1]. Permafrost contains a large organic carbon pool, estimated to be ca.1300 Pg [2]. The rise in global temperatures has accelerated the thawing of this permafrost, causing an expansion in the number and size of thermokarst lakes in

certain northern regions, with an associated mobilization of organic carbon and its decomposition via diverse microbial processes [3,4]. The existence of anaerobic conditions favors the methanogenesis of organic matter into CH<sub>4</sub> [5] that, along with the emitted CO<sub>2</sub>, may have a positive feedback on climate warming [6]. Permafrost thawing and the associated release of organic matter may also mobilize contaminants, such as mercury [7].

Dissolved organic matter (DOM) is composed of a complex mixture of organic compounds with widely varying composition, structural characteristics, and functional groups, depending on its age and origin [8,9]. Variations of structural properties and functional groups in DOM samples can provide insights into the biogeochemical processes taking place within the studied system. DOM of greater availability to microbial degradation (labile organic matter) is likely to be a highly variable fraction of total DOM, but few studies to date have focused on the link between the structural and chemical characteristics of DOM and their bio-lability, particularly in methane emitting thermokarst lake systems.

Given the heterogeneity of DOM, a wide range of analytical techniques is necessary to achieve its characterization fully. Recent studies have focused on different processes of DOM degradation (microbial transformation, photodegradation) and the effects on chemical and structural properties of DOM [10,11]. DOM composition affects its photochemical lability and the resulting photoproducts in natural waters [12], which, in turn, are available for microbial processes. Given the complexity of DOM, a variety of analytical tools are needed to provide structural and functional information. Appropriate spectroscopic techniques have included Fourier-transform infrared (FTIR), molecular fluorescence, and nuclear magnetic resonance (NMR) to understand better the origin and sources of DOM in natural waters [13–15].

Peatland thaw lakes are an important class of thermokarst waters that occur in many permafrost landscapes of the Arctic and subarctic and are characterized by high concentrations of DOM and strong emissions of greenhouse gases, especially methane [16]. In the present work, we focused on a set of peatland permafrost lakes and ponds in subarctic Quebec, where permafrost thawing has been proceeding rapidly [17]. Specifically, we addressed the questions: What are the general DOM characteristics of these blackwater lakes, and are there differences with depth and among lakes? We addressed these questions by way of analysis of DOM samples from three thermokarst lakes at different depths using a suite of methods, specifically liquid-state <sup>1</sup>H and <sup>1</sup>H-<sup>13</sup>C heteronuclear single quantum correlation (HSQC) NMR, FTIR coupled to attenuated total reflectance (FTIR-ATR), fluorescence spectroscopy, and elemental analysis.

## 2. Materials and Methods

### 2.1. Study Sites

The Sasapimakwananisikw (SAS) River valley is located 8 km southeast of Kuujjuarapik–Whapmagoostui (Nunavik, Canada). It is in the sporadic permafrost zone and has abundant lakes and ponds that are formed in a peatland containing palsas (permafrost mounds), which collapse and deliver organic matter previously trapped in permafrost into the aquatic ecosystem (landscape details at this site are shown in Figure 7 in [18]). These palsas are thawing and degrading rapidly due to increasing soil and air temperatures [19]. Lake SAS 2A (55°13'35.6 N, 77°41'49.1 W) is located on the north margin of the SAS river, while Lake SAS 1A (55°13'07.7 N, 77°42'28.4 W) and Lake SAS 1B (55°13'08.3 N, 77°42'29.6 W) are on the south side of the river (Figure 1).

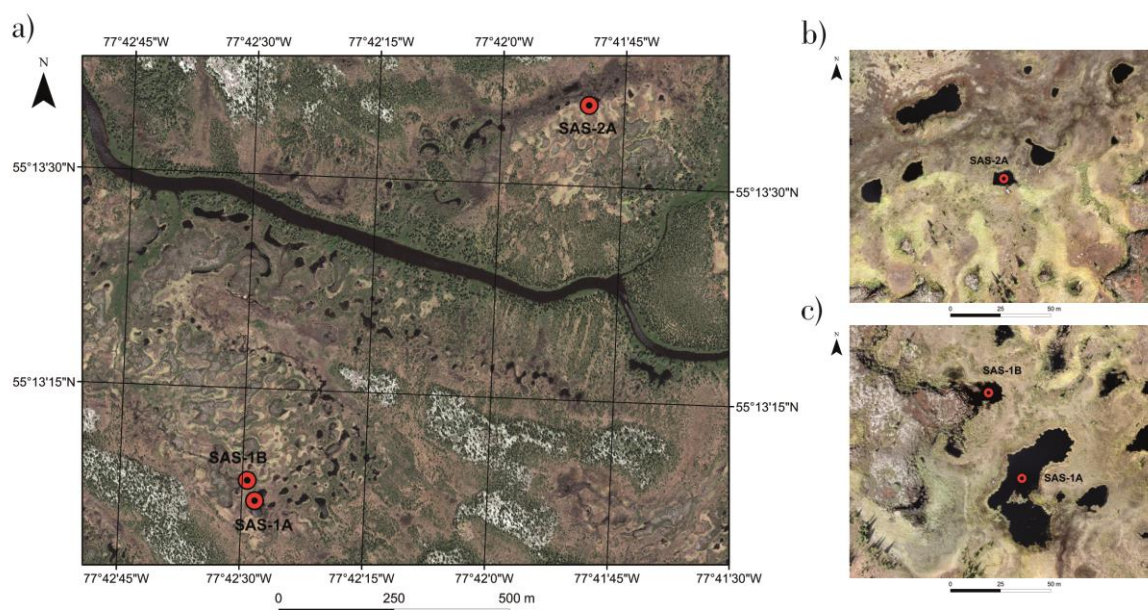


**Figure 1.** Regional (a) and detailed (b,c) location of lakes SAS-2A, SAS-1B and SAS-1A in the Sasapimakananikw (SAS) River valley, subarctic Québec, Canada. Source: Esri, DigitalGlobe, GeoEye, Earthstar Geographics, CNES/Airbus DS, USDA, USGS, AeroGRID, IGN, and the GIS User Community (a) and Unmanned Aerial System surveys from 1 September 2017 (b,c).

Lake SAS 1A has an exposed water surface area of 1661 m<sup>2</sup> and a depth of 1.3 m, surrounded by a dense macrophyte population of the sedge *Carex aquatilis* growing on a surface layer of recent peat during the warm season [17]. Lake SAS 1B, located directly attached to the palsa, has a surface area of 491 m<sup>2</sup> and a depth of 0.6 m. Although of greater depth (2.5 m), lake SAS 2A has an area of only 104 m<sup>2</sup>, with surrounding macrophytes as at SAS 1A.

## 2.2. Sampling

Sampling took place in the SAS valley at the end of winter, March 2018, given the lack of winter limnology of northern lakes despite the importance for greenhouse gas production at this time [20], and also because higher concentrations of DOM are likely to occur during this cold water season without meltwater flushing [21]. Three thermokarst lakes were sampled: lakes SAS 1A, SAS 1B, and SAS 2A. Lake SAS 1A (max. depth 1.3 m) and SAS 2A (max. depth 2.5 m) were sampled at the surface (just below the ice) and bottom (ca. 5 cm above the sediment), while SAS 1B was sampled at medium depth since the total water column was less than 60 cm.

Before sampling, the following physicochemical properties in the water below the ice were measured with a Hydrolab DS5 multi-probe sensor (OTT Hydromet): temperature (°C), pH, specific conductivity (μS cm<sup>-1</sup>), and dissolved oxygen (% air equilibrium and mg L<sup>-1</sup>). Total dissolved solids and salinity estimates were derived from specific conductivity (normalized to 25 °C).

For water sampling, pre-cleaned 2.5 L amber glass containers were used. Each container was previously decontaminated: first, it was immersed in a NaOH (0.1 M) solution for 1 h, then left in HNO<sub>3</sub> (4.0 M) overnight, after which it was thoroughly washed with Milli-Q water. Before sampling, these containers were rinsed three times with lake water to minimize contamination further. Each water sample (2.2 L) was collected with a Masterflex peristaltic pump. Upon collecting the water samples, these were maintained in refrigerated conditions (and protected from light) until they were transported to the laboratory, where the sample treatment was promptly conducted.

Table 1 contains the approximate snow depth and ice thickness, as well as the sampling depth in all three thaw lakes.

**Table 1.** Surface, medium, and bottom sampling depths for SAS 1A, SAS 1B, and SAS 2A, as well as the corresponding snow depth and ice thickness of each site.

	SAS 1A	SAS 2A	SAS 1B
Snow depth	0.5 m	0.5 m	0.5 m
Ice thickness	1.0 m	1.0 m	0.5 m
Surface lake depth	just below the ice	just below the ice	-
Medium lake depth	-	-	0.3 m
Bottom lake depth	1.3 m	2.5 m	-

### 2.3. Methods

#### 2.3.1. Sample Filtration

Water samples were pre-filtered using Whatman<sup>®</sup> glass microfiber GF/F filters (GE Healthcare UK Limited, Amersham Place, Little Chalfont, Buckinghamshire HP7 9NA, UK) (nominal pore size of 0.7  $\mu\text{m}$ ) to remove the larger particulate matter and then filtered through a Durapore<sup>®</sup> PVDF membrane filter (Merck Milipore Ltd., Tullagreen, Carrigtwohill, Co. Cork, Ireland) (0.45  $\mu\text{m}$  pore size). The DOM fractions were acidified to pH 2.5 through the addition of HCl (30%), resulting in the flocculation of a portion of organic matter (commonly referred to as humic acids). To separate the flocculated fraction from the dissolved fraction, the samples were centrifuged at 6000 rpm for 20 minutes.

The recovered supernatant liquid has undergone solid-phase extraction (SPE) using a PPL resin (the commercial name of a styrene-divinylbenzene (SDVB) polymer modified with a proprietary non-polar surface) for DOM extraction before characterization, following the method described by Dittmar et al. 2008 [22]. Upon extraction, the PPL-DOM samples were freeze-dried and kept on a desiccator over silica gel for further analysis.

#### 2.3.2. Dissolved Organic Carbon Quantification

Dissolved organic carbon (DOC) quantification in each sample was conducted through a UV-persulfate oxidation method as described by Lopes et al., 2006 [23], in a Skalar (Breda, The Netherlands) San++ Automated Wet Chemistry Analyzer. The water used to prepare each necessary reagent was bubbled with N<sub>2</sub> gas to remove all inorganic carbon before DOC analysis. The data regarding the DOC detection of the different fixation processes are expressed in the Supporting Material section, containing the calibration curves, slopes, and intercept, as well as the confidence interval for both and the detection limits.

#### 2.3.3. Excitation–Emission Matrix Fluorescence Spectroscopy

Fluorescence spectra were obtained on a JASCO spectrophotometer, model FP-6500, recording individual emission spectra from 250 to 600 nm at sequential increments of 10 nm of excitation wavelength between 225 and 450 nm. The spectra were recorded at a scan speed of 1000 nm min<sup>-1</sup> using emission and excitation bandwidths of 5 nm. For each day of analysis, the instrument was auto-zeroed before each measurement, and a spectrum of a sample of ultra-pure water was acquired under the same experimental conditions and used as blank. A 1 cm path-length quartz cuvette was used in all fluorescence measurements. Five excitation–emission matrices (EEMs) were obtained for the five DOM samples, prior to and after acidification. Rayleigh and Raman scattering were eliminated by using a blank and through post-processing of the obtained EEM data in MATLAB<sup>®</sup> by removing the scattering bands and filling these regions by interpolation of the surrounding data points [24]. The EEMs of each DOM sample before acidification are displayed in the Supporting Material.

The calculated humification index (HIX) values are an approximation of the HIX equation [25], as the obtained EEMs were obtained at an excitation wavelength interval of 5 nm and the emission wavelength interval of 2 nm. Considering this, an estimate of HIX was obtained by using an excitation wavelength of 255 nm, for an emission interval of both 300–346 nm and 434–480 nm, instead of using

the excitation wavelength at 254 nm, in an emission interval of both 300–345 nm and 435–480 nm [26]. The use of this characterization technique allows the evaluation of the properties of fluorescence DOM, providing insight into their origin and lability.

#### 2.3.4. FTIR Spectroscopy

All FTIR-ATR spectra were acquired on a Perkin Elmer FTIR spectrophotometer (FTIR System Spectrum BX) in the 4000–500  $\text{cm}^{-1}$  region. The spectral resolution was 4  $\text{cm}^{-1}$ , and 64 scans were averaged.

#### 2.3.5. NMR Spectroscopy

NMR spectra were acquired using a Bruker Avance-500 spectrometer operating at 500.13 MHz for  $^1\text{H}$  and 125.77 MHz for  $^{13}\text{C}$  and equipped with a liquid nitrogen cooling CryoProbe Prodigy™. The freeze-dried PPL-DOM samples were dissolved in  $\text{D}_2\text{O}$  in 5 mm NMR tubes before NMR analysis. Employing structural characterization techniques (FTIR and NMR) allowed for greater insight into the structural properties that comprise the complex mixture of DOM of each different sample, enabling a greater comprehension of the biogeochemical processes that are involved in each thaw lake.

#### 2.3.6. Elemental Analysis

Elemental analysis of PPL-DOM samples was performed with a Truspec 630-200-200 CHNS, St. Joseph, MI, USA analyzer, with the elemental detection of carbon and hydrogen through IR absorption and the elemental detection of nitrogen by means of thermal conductivity. Triplicate analyses were performed for each sample. Obtaining elemental analysis data on DOM samples can provide valuable information about their properties and nature.

### 3. Results and Discussion

#### 3.1. DOC Quantification

DOC concentrations were obtained by duplicate measurements of each sample of all filtered samples from thermokarst lakes (Table 2). These measurements showed relatively lower and more evenly distributed DOC content in SAS 1A samples, while SAS 2A S (S: Surface sample) and SAS 2A B (B: Bottom sample) appeared to display a significantly higher DOC difference, probably arising from stratification within the lake.

**Table 2.** Table containing the average C content in  $\text{mg C L}^{-1}$  ( $\pm\text{SD}$ ) for each of the dissolved organic matter (DOM) samples. S: surface samples; M: medium depth samples; B: bottom samples.

Lake Sample	Depth (m)	Average C Content ( $\text{mg C L}^{-1}$ )
SAS 1A S	Just below the ice	$18.8 \pm 0.9$
SAS 1A B	1.3 m	$18.0 \pm 0.4$
SAS 2A S	Just below the ice	$22.6 \pm 0.9$
SAS 2A B	2.5 m	$31.5 \pm 0.5$
SAS 1B M	0.3 m	$36.4 \pm 0.5$

#### 3.2. Physicochemical Profiles

The vertical profiles showed vertical gradients in temperature, pH, electrical conductivity, and dissolved oxygen in all three thaw lakes (Figure 2).

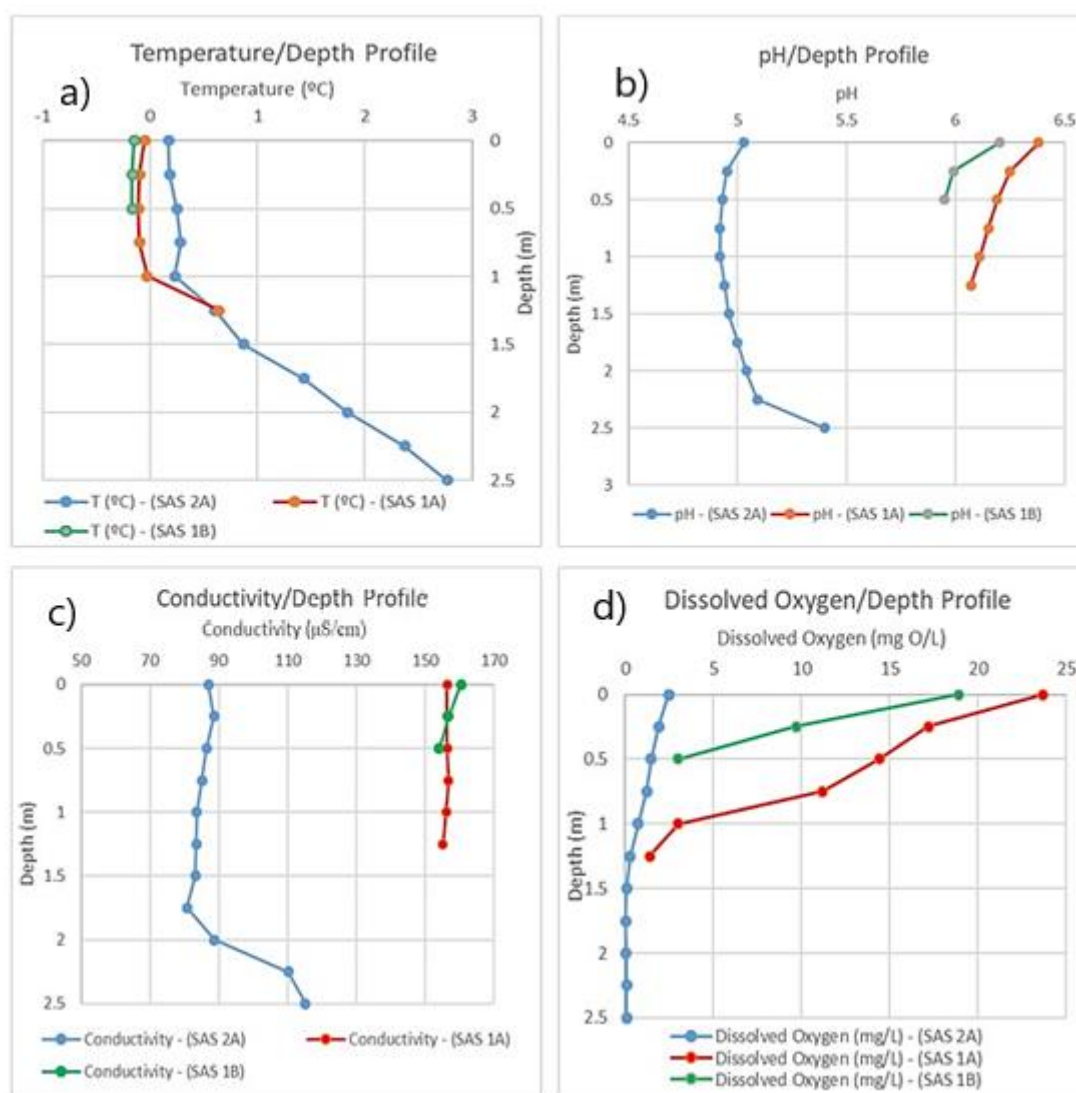


**Figure 2.** Vertical profiles of physicochemical variables. Blue: Lake SAS 2A; Red: Lake SAS 1A; Green: Lake SAS 1B. (a) Temperature; (b) pH; (c) Electrical conductivity; (d) Dissolved oxygen. The lower ice surface was set as 0 m depth for all cases.

Little temperature variation was observed down the shallow water column of SAS 1B; however, Lake SAS 1A maintained a relatively stable temperature (slightly below 0 °C) until a depth of 1 m, then rapidly increased for the remaining 25 cm of depth. A similar trend was observed in Lake SAS 2A (with a surface temperature of 0.17 °C), with an almost linear increase in temperature at depths below 1 m.

All the waters were acidic; however, Lake SAS 2A had a considerably lower pH than the other waters (Figure 2b). The pH levels decreased until 1 m depth; however, pH values increased at greater depths in Lake SAS 2A.

The vertical profile of electrical conductivity (Figure 2c) showed that lakes SAS 1A and SAS 1B had considerably higher inorganic solute concentrations than Lake SAS 2A. The profiles varied little with depth, however below 2 m in Lake SAS 2A, there was a rise in electrical conductivity, suggesting greater salt release by prolonged mineralization in deeper waters and sediments.

The dissolved oxygen profiles (Figure 2d) indicated greater oxygen levels for lakes SAS 1A and SAS 1B near the surface; however, these values were likely due to the invasion of oxygen from the atmosphere through the drill hole. All lakes showed a rapid drop to anoxic conditions at depth, which would be conducive to microbial degradation of labile DOM into methane.

### 3.3. Excitation–Emission Matrix Fluorescence Spectroscopy

Fluorescence spectra EEMs obtained for the DOM samples showed two main peaks in all samples, peak A and peak C, associated with humic-like substances [27,28]. The majority of EEMs of DOM SAS samples (after acidification) had similar spectra; however, SAS 1A S had an intense peak T, associated with microbially-derived DOM [27,28] (Figure 3).

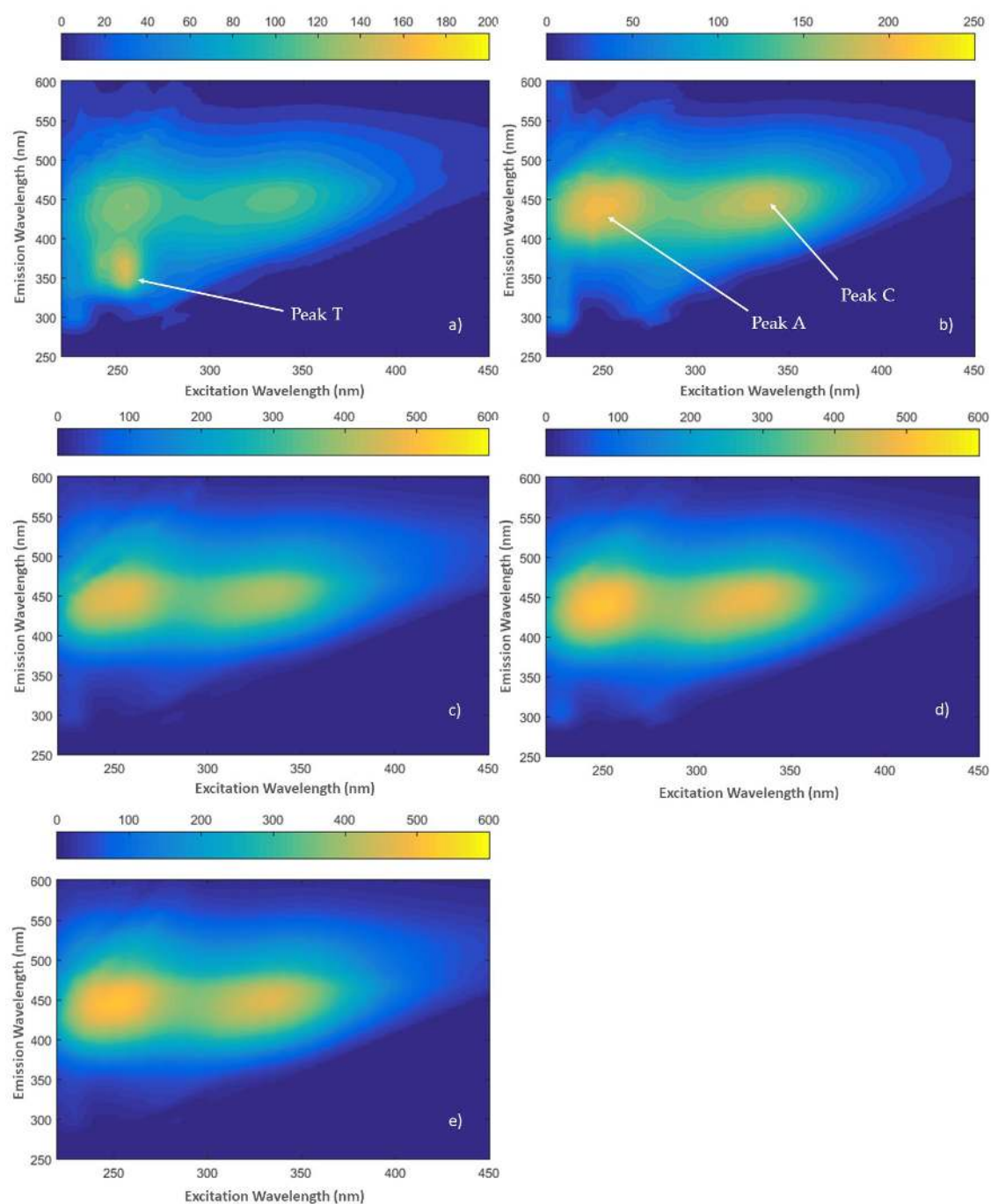


**Figure 3.** Fluorescence excitation–emission matrices (EEMs) of SAS DOM samples after acidification; (a) SAS 1A surface; (b) SAS 1A bottom; (c) SAS 2A surface; (d) SAS 2A bottom; (e) SAS 1B mid-water column.

In an attempt to gather further information regarding the properties and origins of the DOM at each site, the fluorescence EEMs were studied and used to calculate several fluorescence indices.

Peak ratios C:A, C:T, and A:T were estimated [29], as well as the humification index (HIX) [25], fluorescence index (FI) [30], biological index (BIX), and the freshness index ( $\beta:\alpha$ ) [29], all shown in Table 3.

**Table 3.** Calculated ratios and indexes for acidified DOM samples from surface (S), middle (M), and bottom (B) samples.

Parameter	SAS 1A S	SAS 1A B	SAS 2A S	SAS 2A B	SAS 1B M
C:A ratio	0.88	0.89	0.87	0.94	0.90
C:T ratio	0.74	5.7	9.7	7.0	13
A:T ratio	0.83	3.7	11	7.4	14
HIX	1.8	7.2	19	11	18
FI	1.6	1.7	1.4	1.6	1.5
BIX	0.55	0.52	0.35	0.49	0.39
$\beta:\alpha$	0.55	0.52	0.34	0.48	0.38

The C:T and A:T ratios were lowest for SAS 1A S and highest for SAS 1A B. For SAS 2A B, however, the C:T and A:T ratio were lower than those for the SAS 2A S sample. Low C:T and A:T peak ratios for Lake SAS 1A may be associated with microbial DOM at the surface of the thaw lake.

The C:T and A:T peak ratios were consistent with the HIX values (Table 3), and suggested that the acidified DOM SAS 1A S, SAS 1A B, and SAS 2A B had a lower degree of humification compared to SAS 2A S and SAS 1B M. Higher HIX values indicate a higher degree of humification, which is associated with a decrease in bioavailability of labile DOM [31]. In this sense, we could expect a greater bioavailability at SAS 1A (particularly the surface) and at the bottom of SAS 2A. It has also been reported that enhanced bacterial production has been associated with decreasing HIX and increasing  $\beta:\alpha$  values [32,33], further indicating a lower microbial contribution in SAS 2A S and SAS 1B M due to decreased bioavailability of labile DOM.

The lowest FI values were obtained for SAS 2A S and SAS 1B M, while the remaining samples had FI values between 1.61 and 1.68 (Table 3). These values suggest a mixed origin of these DOM fractions [30]. In both SAS 1A and SAS 2A, the bottom samples displayed higher FI values than the corresponding surface sample, indicating a more microbial origin to FDOM in these samples. Recent studies have pointed out that FI values tend to decrease when the production of methane ceases [31,34], suggesting autochthonous DOM may act as one of the primary sources for methanogenesis. Therefore, SAS 1A was expected to possess greater methanogenic potential than SAS 2A and SAS 1B. However, it is also possible that the decreased labile DOM content measured in SAS 2A S and SAS 1B M is a result of the rapid degradation of this fraction, producing and releasing greenhouse gases, leading to a lower FI value.

BIX and  $\beta:\alpha$  displayed a similar trend in all samples since both indices are related to the proportion of recently produced DOM ( $\beta:\alpha$ )/autotrophic productivity (BIX) [32,35] to older and more terrestrial DOM [36]. The values obtained suggest SAS 1A samples and SAS 2A B had more recently produced DOM (likely resulting from microbial activity) than SAS 2A S and SAS 1B M. The BIX and  $\beta:\alpha$  values of SAS 1A were greater at the surface than at the bottom, possibly arising from the surface leaching of labile organic matter from emergent macrophytes that proliferate in the surrounding environments during the warm season, as revealed in automated camera images from this site throughout the year [16,37].

#### 3.4. FTIR-ATR Spectra of PPL-DOM Samples

The FTIR-ATR spectra from 4000 and 500  $\text{cm}^{-1}$  indicated strong similarities among all PPL-DOM samples (Figure 4), indicating strong similarities in composition. There were major bands in all spectra at 3500–3000  $\text{cm}^{-1}$  (H-bonded OH stretching of phenol, hydroxyl, and carboxyl groups) [38], 2960  $\text{cm}^{-1}$  (C-H stretching of methyl and methylene groups of aliphatic chains) [38,39], 1717  $\text{cm}^{-1}$  (unconjugated C=O stretching mainly of carboxyl groups and, in a lesser extent, of ketones and



aldehydes) [13,40],  $1390\text{ cm}^{-1}$  (may arise due to O-H bending in carbohydrates) [13],  $1220\text{ cm}^{-1}$  (in-plane O-H bending vibrations in lignin-derived structures) [13,40], and  $1050\text{ cm}^{-1}$  (C-O asymmetric stretching of carbohydrate moieties and ethers) [13,38].

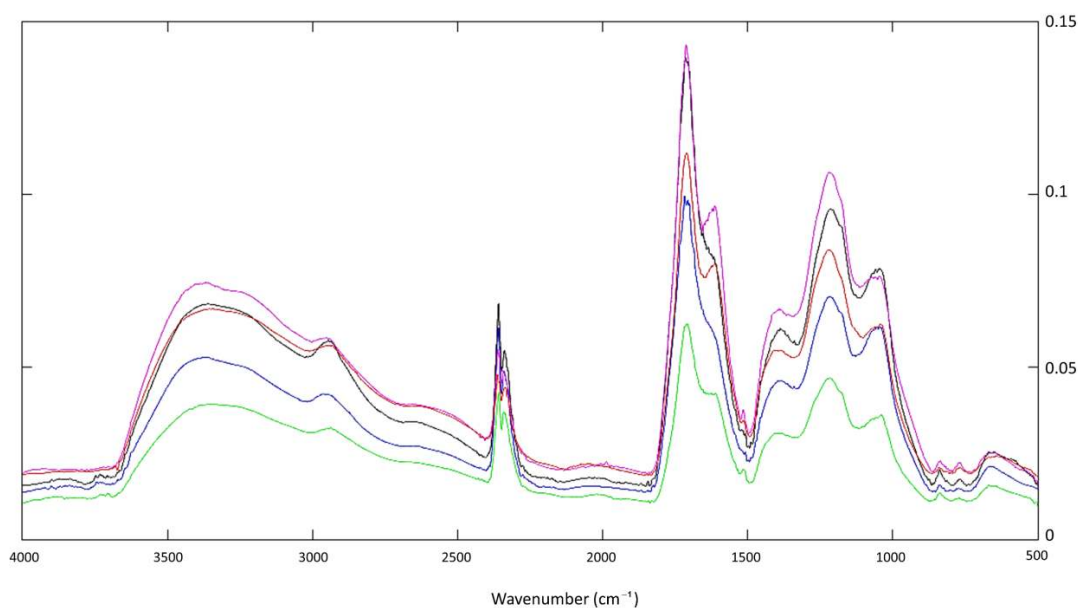


**Figure 4.** Fourier-transform infrared spectroscopy–attenuated total reflectance (FTIR-ATR) spectra of all PPL-DOM SAS samples. Black: SAS 1A B; Blue: SAS 1A S; Green: SAS 2A B; Magenta: SAS 2A S; Red: SAS 1B M.

All samples showed a clear presence of phenols, carboxyl, and/or hydroxyl groups ( $3500\text{--}3000\text{ cm}^{-1}$ ), as the carboxyl presence was also attested by the band at  $1717\text{ cm}^{-1}$ . Similarly, the presence of carbohydrates in all samples was suggested by the bands at  $1390$  and  $1050\text{ cm}^{-1}$ , as well as aromatic moieties (band at  $1220\text{ cm}^{-1}$ ), possibly arising from lignin-derived compounds, in all of the samples.

In the range of  $3000$  to  $2800\text{ cm}^{-1}$ , there was a clearly noticeable peak at  $2960\text{ cm}^{-1}$ , generally associated with C-H methyl and methylene in aliphatic chains [38,39]. In PPL-DOM SAS 1A samples, particularly SAS 1A B, there appeared to be a slightly more well-defined band than in SAS 2A and 1B samples, suggesting a greater aliphatic content in 1A samples.

The band situated at  $1717\text{ cm}^{-1}$  was attributed to the unconjugated C=O stretching mainly of carboxyl groups and, to a lesser extent, of ketones and aldehydes [13,40]. However, the band located at  $1626\text{ cm}^{-1}$  (associated with the C-C stretching of aromatic rings and to C=O stretching of conjugated carbonyl groups) [41], while clearly defined in PPL-DOM SAS 2A S and SAS 1B M samples, showed a shoulder-like form for PPL-DOM SAS 2A B and 1A samples, indicating a lower aromatic or carbonyl presence in these samples when compared to SAS 2A S and SAS 1B M.

The spectra of PPL-DOM SAS 1B and SAS 2A samples also exhibited a relatively well-defined band at approximately  $1515\text{ cm}^{-1}$  (C-C stretching vibrations of aromatic rings), characteristic of lignin-derived structures [42,43]. PPL-DOM SAS 1A samples did not display that as a well-defined band, indicating that SAS 2A and 1B samples had a greater lignin content. All SAS spectra displayed peaks at  $1390\text{ cm}^{-1}$  (likely arising from the presence of carbohydrates), at  $1220\text{ cm}^{-1}$  (associated with lignin-derived moieties) [13], and at  $1050\text{ cm}^{-1}$  (emerging from polysaccharides and polysaccharide-like compounds, such as cellulose) [38]. It should be noted that in PPL-DOM SAS 1A samples, since the band centered at  $1050\text{ cm}^{-1}$  appeared to be more defined than in SAS 2A and 1B samples, the possibility of a greater polysaccharide content in SAS 1A becomes plausible [38]. The possibility of a higher polysaccharide content in SAS 1A would signify higher DOM lability. This would be in accordance with the increased microbial activity indicated in the fluorescence EEMs.

### 3.5. Liquid-State $^1\text{H}$ NMR Spectra of PPL-DOM Samples

Figure 5 shows the liquid-state  $^1\text{H}$  NMR spectra of all PPL-DOM samples. Four main categories of functional groups carrying C-H bonds can be identified in these spectra [44–46]:  $\delta_{\text{H}}$ : 0.6–1.9 ppm (protons bound to carbon atoms of straight and branched aliphatic chains (C-H), which included protons from methyl (R-CH<sub>3</sub>), methylene (R-CH<sub>2</sub>), and methyne (R-CH) groups,  $\delta_{\text{H}}$ : 1.9–3.2 ppm (protons bound to carbon atoms in  $\alpha$ -position to unsaturated groups in allylic (H-C <sub>$\alpha$</sub> -C=) (generally referred to as CRAM (carboxyl-rich alicyclic molecules)), carbonyl or amino (H-C <sub>$\alpha$</sub> -C=O or H-C <sub>$\alpha$</sub> -C=N) groups, protons from methyl groups bound to an aromatic carbon, and protons in secondary and tertiary amines (H-C-NHR and H-C-NR<sub>2</sub>),  $\delta_{\text{H}}$ : 3.5–4.5 ppm (protons bound to oxygenated saturated aliphatic carbon atoms (H-C-O) in alcohols, polyols, ethers, esters, and organic nitrate (R-CH<sub>2</sub>-O-NO<sub>2</sub>)), and  $\delta_{\text{H}}$ : 6.5–8.4 (protons bound to aromatic carbon atoms (Ar-H)). Additional NMR resonance at  $\delta_{\text{H}}$ : 5.0–5.5 ppm, assigned to protons bound to anomeric carbons [O-C(H)-O], was also apparent in all spectra.

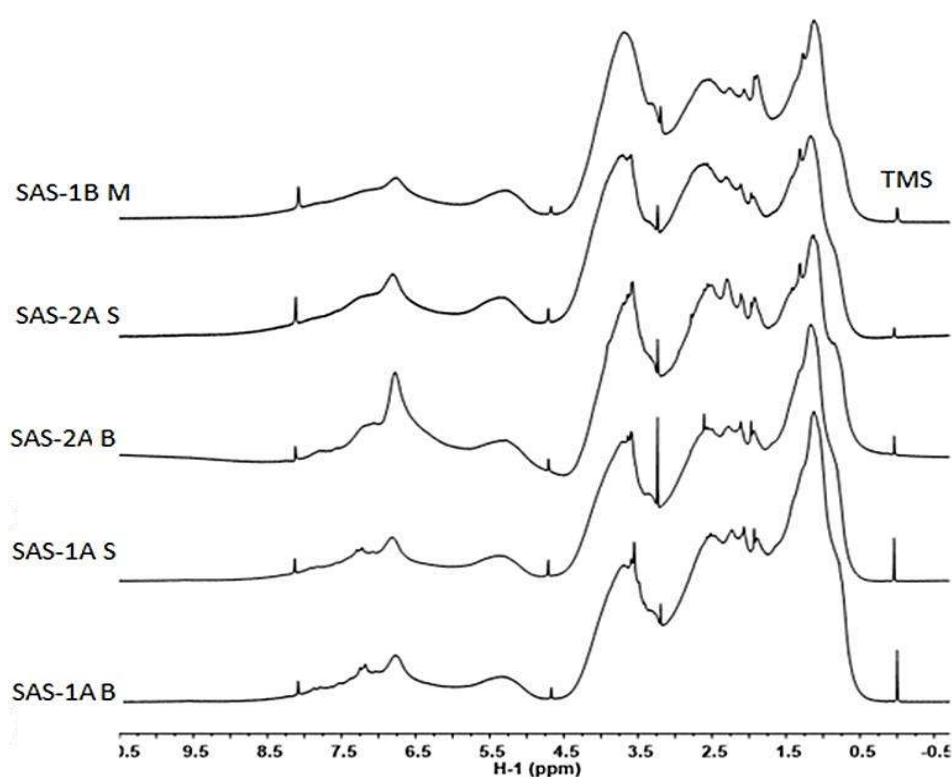


**Figure 5.** Liquid-state  $^1\text{H}$  NMR spectra of all PPL-DOM SAS samples. Chemical shifts were referenced in Table 1.  $^1\text{H}$  NMR spectra were similar and indicated a relatively low aromatic content compared to peptide/carbohydrate, carboxyl-rich alicyclic molecules (CRAM), and aliphatic content. However, certain structural differences between samples became more discernible upon closer examination.

PPL-DOM SAS 1A samples exhibited a higher relative intensity in the  $\delta_{\text{H}}$ : 0.6–1.9 region, indicating a higher aliphatic content in these samples, possibly a result of microbial transformation within SAS 1A [47]. Moreover, a peak was apparent at approximately  $\delta_{\text{H}}$ : 6.75 ppm, particularly in the spectrum of PPL-DOM SAS 2A B sample, attributable to the presence of lignin [48], indicating the possibility of a greater lignin presence at the bottom of lake SAS 2A. This higher aromatic content might not only be due to the contribution of thawing permafrost but may also be related to the fact that SAS 2A is the deepest sampled thaw lake, which would lead to a lesser degree of photodegradation of photolabile aromatic compounds [10].

In the region of  $\delta_{\text{H}}$ : 7.0–7.5 ppm, a clearly noticeable peak occurred in the analyses of both SAS 1A samples; specifically, there was a shoulder-like band in the SAS 2A B sample, which is

commonly associated with aromatic amino acid side chains [49], and suggesting the possibility of higher aromatic-protein content in SAS 1A.

### 3.6. Liquid-State $^1\text{H}$ - $^{13}\text{C}$ HSQC NMR spectra of PPL-DOM Samples

The  $^1\text{H}$ - $^{13}\text{C}$  HSQC NMR spectrum of PPL-DOM SAS 1A S (Figure 6a) was divided into five major spectral regions [50–52]: Region I ( $\delta_{\text{H}}$ : 0.5–1.5 ppm and  $\delta_{\text{C}}$ : 10–30 ppm – assigned to purely aliphatic groups), II (ca.  $\delta_{\text{H}}$ : 1.5–3.5 ppm and  $\delta_{\text{C}}$ : 30–45 ppm – assigned to CRAM), III (ca.  $\delta_{\text{H}}$ : 3.0–4.0 ppm and  $\delta_{\text{C}}$ : 50–65 ppm, containing a noticeable cross peak at  $\delta_{\text{H}}$ : 3.25–3.80 ppm and ca.  $\delta_{\text{C}}$ : 50 ppm – assigned to aromatic methoxyl groups (Ar-O-CH<sub>3</sub>) [53] indicating the presence of ethers and esters), IV (ca.  $\delta_{\text{H}}$ : 3.25–4.5 ppm and  $\delta_{\text{C}}$ : 65–80 ppm – assigned to carbohydrates) [15,32,54], and V (ca.  $\delta_{\text{H}}$ : 6.25–7.5 ppm and  $\delta_{\text{C}}$ : 115–135 ppm – aromatic regions, likely representing oxygenated aromatic structures) [15,47].

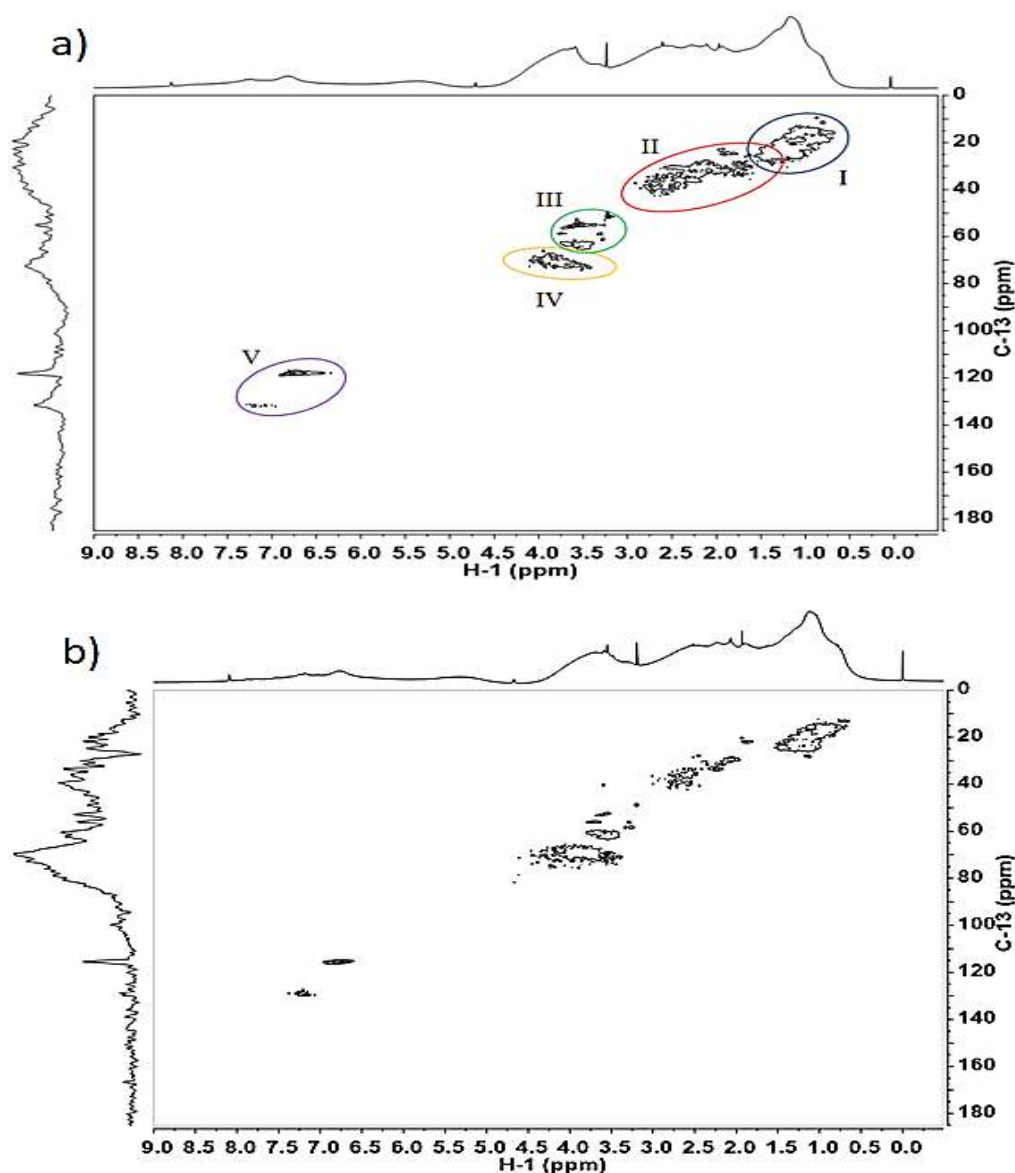
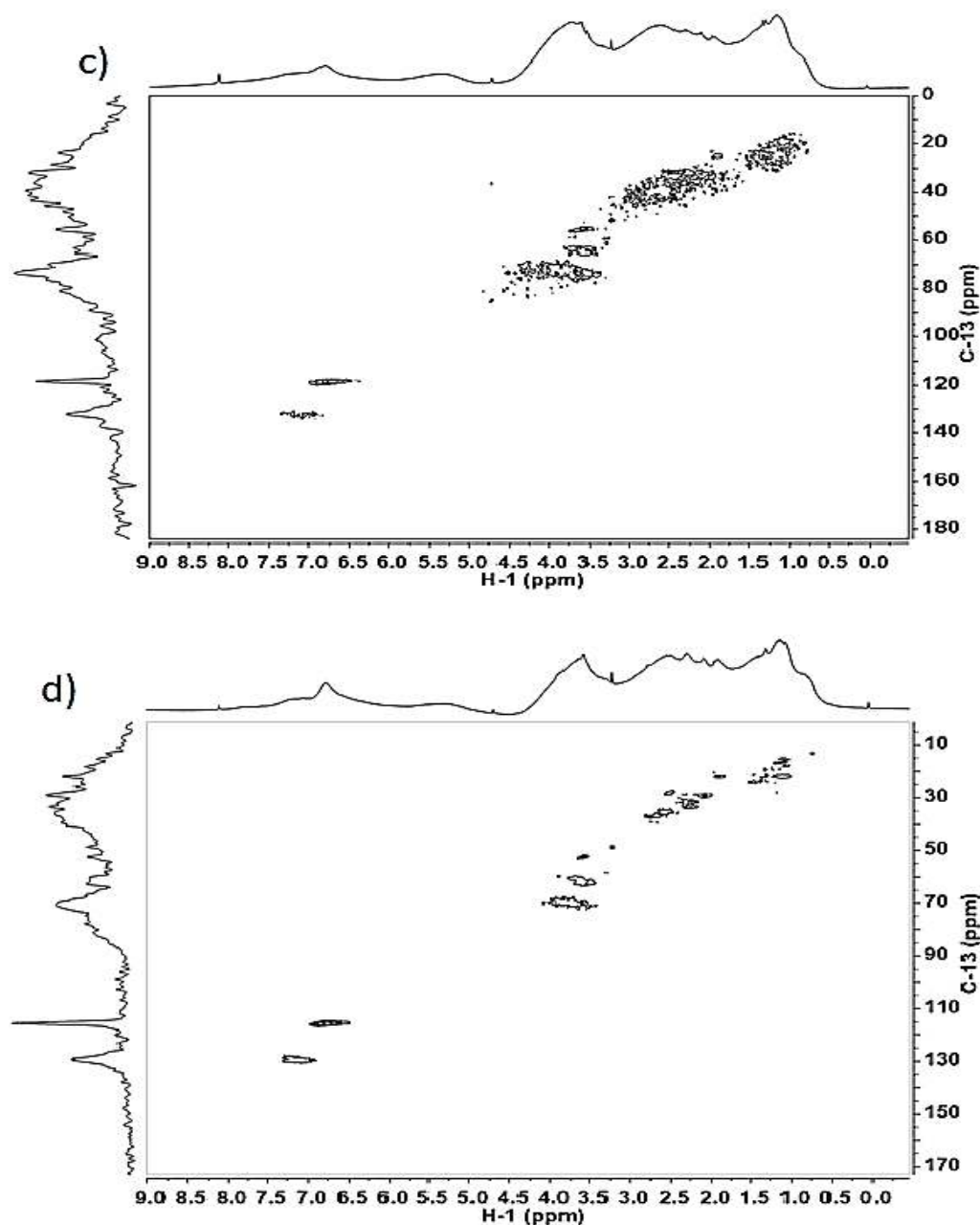


Figure 6. Cont.



**Figure 6.**  $^1\text{H}$ - $^{13}\text{C}$  HSQC NMR spectra of (a) PPL-DOM SAS 1A S, (b) PPL-DOM SAS 1A B, (c) PPL-DOM SAS 2A S, and (d) PPL-DOM SAS 2A B. Five specific spectral regions are highlighted in the spectrum of PPL-DOM SAS 1A S: Region I (blue)—Aliphatic moieties; Region II (red)—CRAM fraction; Region III (green)—ethers and esters; Region IV (yellow)—carbohydrate moieties; Region V (purple)—aromatic molecules.

All  $^1\text{H}$ - $^{13}\text{C}$  HSQC NMR spectra showed that the PPL-DOM SAS samples were dominated by aliphatic, carboxyl-rich alicyclic molecules (CRAM) and carbohydrate moieties. In both SAS 2A and SAS 1A samples, the overall HSQC cross-peaks positioning displayed closer similarities to the chemical signatures with microbially-derived origin DOM than with plant-derived DOM [47], indicating some degree of microbial transformation on both SAS 1A and SAS 2A samples. The lack of cross-peaks in the acetyl region of the HSQC spectra, a region commonly linked to the presence of biomolecules, such as peptidoglycan, originating from bacterial cell walls [55], may be associated with photodegradation (given its propensity to undergo photodegradation) [49]. PPL-DOM SAS 1A samples displayed a greater variety of aliphatic compounds at  $\delta_{\text{H}} < 1.0$  ppm and  $\delta_{\text{C}} < 20$  ppm compared to SAS 2A samples,

generally assigned to non-cyclic aliphatics [56], likely arising from the microbial transformation of labile DOM [47], originating methyl-terminating purely aliphatic units in peptide side chains or common lipids [57]. The HSQC spectra (Figure 6c,d) showed a significantly greater molecular diversity of methyl groups, CRAM, and O-alkyl regions in SAS 2A S compared to SAS 2A B, further underscoring the stratification and vertical heterogeneity within this lake.

Both surface samples of SAS 1A and SAS 2A appear to show greater chemical diversity than their respective bottom samples, particularly in the case of SAS 2A. This may be due to the formation of new organic compounds arising from photodegradation [10] or microbial transformation [47]. There may also be a contribution from macrophyte leachates at the surface of these permafrost thaw lakes, which, when exposed to microbial degradation (and photodegradation), would further increase the molecular diversity in the DOM mixture, as indicated in the HSQC spectra.

Comparing the surface samples of PPL-DOM SAS 1A and SAS 2A, we found a greater number of methyl group cross-peaks in SAS 1A S, particularly at lower chemical shifts than in SAS 2A S, suggesting a greater degree of microbial transformation occurring at the surface of SAS 1A [47]. In the bottom samples of SAS 1A and SAS 2A, there was a much greater variety of aliphatic and carbohydrate cross-peaks in SAS 1A B than in SAS 2A B, indicating not only a greater degree of newly produced organic moieties (photodegradation or microbial transformation) in SAS 1A B but also at the increased water column stratification in SAS 2A.

### 3.7. Elemental Analysis of PPL-DOM Samples

The elemental analysis of PPL-DOM SAS samples (Table 4) showed values of the same order of magnitude as those published in the literature for reference Suwannee River fulvic acids [58], Campsite Lake fulvic acids, Island Lake fulvic acids, and Toolik Lake fulvic acids [59].

**Table 4.** Average elemental composition and atomic ratios of PPL-DOM SAS samples.

Sample	C (%)	H (%)	N (%)	H:C	N:C
SAS 1A S	47.0 ± 0.2	4.98 ± 0.21	1.41 ± 0.10	1.26	0.0257
SAS 1A B	48.4 ± 0.5	4.92 ± 0.059	1.30 ± 0.02	1.21	0.0230
SAS 2A S	44.3 ± 0.3	4.15 ± 0.22	1.19 ± 0.01	1.11	0.0230
SAS 2A B	46.4 ± 0.5	4.20 ± 0.19	1.40 ± 0.01	1.08	0.0258
SAS 1B M	48.3 ± 0.6	3.92 ± 0.09	1.35 ± 0.01	0.966	0.0241

The atomic H:C ratio values of PPL-DOM SAS samples varied in the following order: SAS 1A S > SAS 1A B > SAS 2A S > SAS 2A B > SAS 1B M, suggesting a higher aliphatic character of PPL-DOM SAS 1A samples compared to SAS 2A and SAS 1B samples. These findings are in concordance with those derived from the <sup>1</sup>H NMR data. The atomic N:C ratios were similar for all PPL-DOM samples but appear to be higher than those published in the literature for fulvic acids samples from Toolik Lake (atomic N:C ratio of 0.0145), Island Lake (atomic N:C ratio of 0.0179), and Campsite Lake (atomic N:C ratio of 0.0175), three lakes from Arctic regions [59], and higher than the Suwannee River Fulvic Acids (atomic N:C ratio of 0.012), the standard for HS [58]. This higher nitrogen content in PPL-DOM SAS samples may result from the thaw of the underlying permafrost.

## 4. Conclusions

Peatland thermokarst lakes in winter contain anoxic waters beneath the ice, with high concentrations of DOM of both autochthonous and allochthonous origins. A varying microbial contribution was detected in some of the DOM samples, prompting the idea of a different labile matter content and hence, a different methanogenic potential between lakes. We cannot exclude the possibility that all SAS samples could have also undergone some degree of photodegradation, which might account for the chemical diversity found at the surface of these lakes.

Structural characterization techniques ( $^1\text{H}$  NMR and FTIR-ATR) provided additional insight into the compositional differences of DOM among thaw lakes. Overall, the structural information indicates that PPL-DOM SAS 1A samples display a significantly higher aliphatic content, likely resulting from the microbial transformation of labile components while displaying a lower aromatic content. SAS 2A B may contain a greater aromatic content, likely a contribution from thawing permafrost or a result of experiencing less photodegradation at the bottom of lake SAS 2A. Surface samples revealed a greater diversity of compounds than their bottom sample counterparts, possibly arising from photodegradation or leaching from surrounding macrophyte communities, rapidly undergoing microbial degradation.

A stronger microbial DOM contribution in SAS 1A (particularly at the surface) and at the bottom of SAS 2A suggested a greater bioavailability of labile DOM in these samples, hence greater methanogenic potential. However, the less autochthonous nature of SAS 2A S and SAS 1B M could be due to the rapid degradation of the labile DOM in these environments. Assessing the presence of labile organic matter and microbial activity in permafrost thermokarst lakes allows not only to shed light on the production of greenhouse gases in thermokarst systems but to evaluate the potential of each lake to produce these greenhouse gases.

The use of several characterization techniques to obtain information about the PPL-DOM samples provided a greater understanding of the properties of DOM in these lakes and insights into the processes that regulate these thermokarst ecosystems. The ongoing use of complementary characterization techniques will be essential towards understanding the complexity of DOM in natural waters, the biogeochemical processes that control the production and degradation of these materials and to explore the link between lability and structural properties.

**Supplementary Materials:** The following are available online at <http://www.mdpi.com/2073-4441/12/11/3059/s1>, Figure S1.1: Calibration curve obtained to quantify the DOC content in the SAS water samples, Figure S1.2.1: Calibration curve obtained to quantify the DOC content in the SPE process of acidified DOM SAS 1A S and SAS 1A B samples, Figure S1.2.2: Calibration curve obtained to quantify the DOC content in the SPE process of SAS 2A S (replicates 1, 2 and 3), Figure S1.2.3: Calibration curve obtained to quantify the DOC content in the SPE process of SAS 2A S (replicates 4, 5, and 6), Figure S1.2.4: Calibration curve obtained to quantify the DOC content in the SPE process of SAS 2A S (replicates 7, 8, and 9), Figure S1.2.5: Calibration curve obtained to quantify the DOC content in the SPE process of SAS 2A B (replicates 1, 2, 3, and 4), Figure S1.2.6: Calibration curve obtained to quantify the DOC content in the SPE process of SAS 2A B (replicates 5, 6, 7, 8, and 9), Figure S1.2.7: Calibration curve obtained to quantify the DOC content in the SPE process of SAS 1B M (replicates 1, 2, 3, and 4), Figure S1.2.8: Calibration curve obtained to quantify the DOC content in the SPE process of SAS 1B M (replicates 5, 6, 7, 8, and 9), Figure S2.1: Fluorescence EEM of SAS 1A S, prior to acidification, Figure S2.2: Fluorescence EEM of SAS 1A B, prior to acidification, Figure S2.3: Fluorescence EEM of SAS 2A S, prior to acidification, Figure S2.4: Fluorescence EEM of SAS 2A B, prior to acidification, Figure S2.5: Fluorescence EEM of SAS 1B M, prior to acidification, Table S1.1.1: Slope and intercept of the calibration curve, confidence interval for both slope and intercept, and limit of detection (LOD), Table S1.1.2: Dilution factor, average C content of two replicates of each sample and their respective confidence interval, Table S1.2.1: Slope and intercept of the calibration curve, confidence interval for both slope and intercept, and LOD for DOC quantification of SPE of SAS 1A S and SAS 1A B samples, Table S1.2.2: Slope, intercept of calibration curve, confidence interval, and LOD for DOC quantification of SPE of SAS 2A S (replicates 1, 2 and 3), Table S1.2.3: Slope, intercept of calibration curve, confidence interval, and LOD for DOC quantification of SPE of SAS 2A S (replicates 4, 5, and 6), Table S1.2.4: Slope, intercept of calibration curve, confidence interval, and LOD for DOC quantification of SPE of SAS 2A S (replicates 7, 8, and 9), Table S1.2.5: Slope, intercept of calibration curve, confidence interval, and LOD for DOC quantification of SPE of SAS 2A B (replicates 1, 2, 3, and 4), Table S1.2.6: Slope, intercept of calibration curve, confidence interval, and LOD for DOC quantification of SPE of SAS 2A (replicates 5, 6, 7, 8, and 9), Table S1.2.7: Slope, intercept of calibration curve, confidence interval, and LOD for DOC quantification of SPE of SAS 1B M (replicates 1, 2, 3, and 4), Table S1.2.8: Slope, intercept of calibration curve, confidence interval, and LOD for DOC quantification of SPE of SAS 1B M (replicates 5, 6, 7, 8, and 9), Table S1.3: Dilution factor, average C content of all conducted replicates of SAS samples compiled and their respective confidence interval.

**Author Contributions:** Conceptualization, A.C.D.; R.M.B.O.D.; J.C.; W.F.V.; M.P.; D.F.; methodology A.C.D. and R.M.B.O.D.; W.F.V.; M.P.; G.V.; and P.F.; validation, A.C.D.; R.M.B.O.D.; A.M.S.S.; J.C., and D.F.; formal analysis, A.C.D.; R.M.B.O.D.; A.M.S.S.; W.F.V.; M.P.; J.C., and D.F.; investigation, D.F.; R.M.B.O.D.; A.C.D.; J.C., and A.M.S.S.; resources, M.P. and G.V.; data curation, D.F.; A.C.D.; R.M.B.O.D.; J.C., and W.F.V.; writing—original draft preparation, D.F.; J.C.; W.F.V., and A.C.D.; writing—review and editing, D.F.; R.M.B.O.D.; A.C.D.; J.C.; A.M.S.S.; W.F.V.; M.P.; G.V., and P.F.; visualization, D.F.; A.C.D.; R.M.B.O.D., and J.C.; supervision, A.C.D.; R.M.B.O.D.; J.C., and W.F.V.; project administration, A.C.D.; J.C.; W.F.V., and R.M.B.O.D.; funding acquisition, J.C.; A.C.D.; R.M.B.O.D.; M.P., and G.V. All authors have read and agreed to the published version of the manuscript.

**Funding:** This research was funded by the Portuguese Polar Program (PROPOLAR) and by Fundação para a Ciência e Tecnologia through projects UIDB/00100/2020, (CQE, Instituto Superior Técnico), UID/AMB/50017/2019 (CESAM, University of Aveiro), UID/QUI/00062/2019 (QOPNA, University of Aveiro), IF/00798/2015 (Investigator FCT Contract), and the PhD Grant SFRH/BD/145142/2019 to D.F. This project also possible due to the Portuguese NMR network.

**Acknowledgments:** We would like to thank Environment and Climate Change Canada under the Climate Change and Air Pollution (CCAP) program, the Natural Sciences and Engineering Research Council of Canada (NSERC), the project BOND in Sentinel North funded by the Canada Research Excellence Fund (CFREF), the NCE program ArcticNet, and the Centre d'études nordiques (CEN) for field support at the Kuujjuarapik/Whapmagoostui research station. This research is framed within the College on Polar and Extreme Environments (Polar2E) of the University of Lisbon.

**Conflicts of Interest:** The authors declare no conflict of interest.

## References

1. Gruber, S. Derivation and Analysis of a High-Resolution Estimate of Global Permafrost Zonation. *Cryosphere* **2012**, *6*, 221–233. [[CrossRef](#)]
2. Hugelius, G.; Strauss, J.; Zubrzycki, S.; Harden, J.W.; Schuur, E.A.G.; Ping, C.L.; Schirmer, L.; Grosse, G.; Michaelson, G.J.; Koven, C.D.; et al. Estimated Stocks of Circumpolar Permafrost Carbon with Quantified Uncertainty Ranges and Identified Data Gaps. *Biogeosciences* **2014**, *11*, 6573–6593. [[CrossRef](#)]
3. Vigneron, A.; Lovejoy, C.; Cruaud, P.; Kalenitchenko, D.; Culley, A.; Vincent, W.F. Contrasting Winter Versus Summer Microbial Communities and Metabolic Functions in a Permafrost Thaw Lake. *Front. Microbiol.* **2019**, *10*, 1–13. [[CrossRef](#)] [[PubMed](#)]
4. Wauthy, M.; Rautio, M.; Christoffersen, K.S.; Forsstrom, L.; Laurion, I.; Mariash, H.L.; Peura, S.; Vincent, W.F. Increasing Dominance of Terrigenous Organic Matter in Circumpolar Freshwaters Due to Permafrost Thaw. *Limnol. Oceanogr.* **2018**, *3*, 186–198. [[CrossRef](#)]
5. Zimov, S.A.; Voropaev, Y.V.; Semiletov, I.P.; Davidov, S.P.; Prosiannikov, S.F.; Chapin III, F.S.; Chapin, M.C.; Trumbore, S.; Tyler, S. North Siberian Lakes: A Methane Source Fueled by Pleistocene Carbon. *Science* **1997**, *277*, 800–802. [[CrossRef](#)]
6. Schuur, E.A.G.; McGuire, A.D.; Schadel, C.; Grosse, G.; Harden, J.W.; Hayes, D.J.; Hugelius, G.; Koven, C.D.; Kuhry, P.; Lawrence, D.M.; et al. Climate Change and the Permafrost Carbon Feedback. *Nature* **2015**, *520*, 171–179. [[CrossRef](#)] [[PubMed](#)]
7. St Pierre, K.A.; Zolkos, S.; Shakil, S.; Tank, S.E.; St Louis, V.L.; Kokelj, S.V. Unprecedented Increases in Total and Methyl Mercury Concentrations Downstream of Retrogressive Thaw Slumps in the Western Canadian Arctic. *Environ. Sci. Technol.* **2018**, *52*, 14099–14109. [[CrossRef](#)] [[PubMed](#)]
8. Dubinenkov, I.; Flerus, R.; Schmitt-Kopplin, P.; Kattner, G.; Koch, B.P. Origin-Specific Molecular Signatures of Dissolved Organic Matter in the Lena Delta. *Biogeochemistry* **2015**, *123*, 1–14. [[CrossRef](#)]
9. Walker, B.D.; Beaupré, S.R.; Guilderson, T.P.; McCarthy, M.D.; Druffel, E.R.M. Pacific Carbon Cycling Constrained by Organic Matter Size, Age and Composition Relationships. *Nat. Geosci.* **2016**, *9*, 888–891. [[CrossRef](#)]
10. Liu, S.; Feng, W.; Song, F.; Li, T.; Guo, W.; Wang, B.; Wang, H.; Wu, F. Photodegradation of Algae and Macrophyte-Derived Dissolved Organic Matter: A Multi-Method Assessment of DOM Transformation. *Limnologia* **2019**, *77*, 125683. [[CrossRef](#)]
11. Textor, S.R.; Wickland, K.P.; Podgorski, D.C.; Johnston, S.E.; Spencer, R.G.M. Dissolved Organic Carbon Turnover in Permafrost-Influenced Watersheds of Interior Alaska: Molecular Insights and the Priming Effect. *Front. Earth Sci.* **2019**, *7*, 1–17. [[CrossRef](#)]
12. Maizel, A.C.; Li, J.; Remucal, C.K. Relationships between Dissolved Organic Matter Composition and Photochemistry in Lakes of Diverse Trophic Status. *Environ. Sci. Technol.* **2017**, *51*, 9624–9632. [[CrossRef](#)] [[PubMed](#)]
13. Kaal, J.; Cortizas, A.M.; Biester, H. Downstream Changes in Molecular Composition of DOM along a Headwater Stream in the Harz Mountains (Central Germany) as Determined by FTIR, Pyrolysis-GC-MS and THM-GC-MS. *J. Anal. Appl. Pyrolysis* **2017**, *126*, 50–61. [[CrossRef](#)]
14. Park, M.; Snyder, S.A. Sample Handling and Data Processing for Fluorescent Excitation-Emission Matrix (EEM) of Dissolved Organic Matter (DOM). *Chemosphere* **2018**, *193*, 530–537. [[CrossRef](#)]

15. Hertkorn, N.; Harir, M.; Cawley, K.M.; Schmitt-Kopplin, P.; Jaffé, R. Molecular Characterization of Dissolved Organic Matter from Subtropical Wetlands: A Comparative Study through the Analysis of Optical Properties, NMR and FTICR/MS. *Biogeosciences Discuss.* **2015**, *12*, 13711–13765. [[CrossRef](#)]
16. Matveev, A.; Laurion, I.; Deshpande, B.N.; Bhiry, N.; Vincent, W.F. High Methane Emissions from Thermokarst Lakes in Subarctic Peatlands. *Limnol. Oceanogr.* **2016**, *61*, 150–164. [[CrossRef](#)]
17. Vincent, W.F.; Lemay, M.; Allard, M. Arctic Permafrost Landscapes in Transition: Towards an Integrated Earth System Approach. *Arct. Sci.* **2017**, *3*, 39–64. [[CrossRef](#)]
18. Bégin, P.N.; Vincent, W.F. Permafrost Thaw Lakes and Ponds as Habitats for Abundant Rotifer Populations. *Arct. Sci.* **2017**, *3*, 354–377. [[CrossRef](#)]
19. Bhiry, N.; Delwaide, A.; Allard, M.; Bégin, Y.; Filion, L.; Lavoie, M.; Nozais, C.; Payette, S.; Pienitz, R.; Saulnier-Talbot, É.; et al. Environmental Change in the Great Whale River Region, Hudson Bay: Five Decades of Multidisciplinary Research by Centre d'études Nordiques (CEN). *Écoscience* **2011**, *18*, 182–203. [[CrossRef](#)]
20. Matveev, A.; Laurion, I.; Vincent, W.F. Winter Accumulation of Methane and Its Variable Timing of Release from Thermokarst Lakes in Subarctic Peatlands. *Biogeosciences* **2019**, *124*, 3521–3535. [[CrossRef](#)]
21. Leppäranta, M. Lake Water Body in the Ice Season. In *Freezing of Lakes and the Evolution of Their Ice Cover*; Springer: Berlin/Heidelberg, Germany, 2015; pp. 203–244. [[CrossRef](#)]
22. Dittmar, T.; Koch, B.; Hertkorn, N.; Kattner, G. A Simple and Efficient Method for the Solid-Phase Extraction of Dissolved Organic Matter (SPE-DOM) from Seawater. *Limnol. Oceanogr. Methods* **2008**, *6*, 230–235. [[CrossRef](#)]
23. Lopes, C.B.; Abreu, S.; Válega, M.; Duarte, R.M.B.O.; Pereira, M.E.; Duarte, A.C. The Assembling and Application of an Automated Segmented Flow Analyzer for the Determination of Dissolved Organic Carbon Based on UV-Persulphate Oxidation. *Anal. Lett.* **2006**, *39*, 1979–1992. [[CrossRef](#)]
24. Zepp, R.G.; Sheldon, W.M.; Ann, M. Dissolved Organic Fluorophores in Southeastern US Coastal Waters: Correction Method for Eliminating Rayleigh and Raman Scattering Peaks in Excitation—Emission Matrices. *Mar. Chem.* **2004**, *89*, 15–36. [[CrossRef](#)]
25. Zsolnay, A.; Baigar, E.; Jimenez, M.; Steinweg, B.; Saccomandi, F. Differentiating with Fluorescence Spectroscopy the Sources of Dissolved Organic Matter in Soils Subjected to Drying. *Chemosphere* **1999**, *38*, 45–50. [[CrossRef](#)]
26. Cox, L.; Celis, R.; Hermosin, M.C.; Cornejo, J.; Zsolnay, A.; Zeller, K. Effect of Organic Amendments on Herbicide Sorption as Related to the Nature of the Dissolved Organic Matter. *Environ. Sci. Technol.* **2000**, *34*, 4600–4605. [[CrossRef](#)]
27. Coble, P.G. Characterization of Marine and Terrestrial DOM in Seawater Using Excitation-Emission Matrix Spectroscopy. *Mar. Chem.* **1996**, *51*, 325–346. [[CrossRef](#)]
28. Stedmon, C.A.; Markager, S.; Bro, R. Tracing Dissolved Organic Matter in Aquatic Environments Using a New Approach to Fluorescence Spectroscopy. *Mar. Chem.* **2003**, *82*, 239–254. [[CrossRef](#)]
29. Hansen, A.M.; Kraus, T.E.C.; Pellerin, B.A.; Fleck, J.A.; Downing, B.D.; Bergamaschi, B.A. Optical Properties of Dissolved Organic Matter (DOM): Effects of Biological and Photolytic Degradation. *Limnol. Oceanogr.* **2016**, *61*, 1015–1032. [[CrossRef](#)]
30. McKnight, D.M.; Boyer, E.W.; Westerhoff, P.K.; Doran, P.T.; Kulbe, T.; Andersen, D.T. Spectrofluorometric Characterization of Dissolved Organic Matter for Indication of Precursor Organic Material and Aromaticity. *Limnol. Oceanogr.* **2001**, *46*, 38–48. [[CrossRef](#)]
31. Zhang, Z.; Guo, L.; Wang, Y.; Li, F. Degradation and Transformation of Extracellular Polymeric Substances (EPS) and Dissolved Organic Matters (DOM) during Two-Stage Anaerobic Digestion with Waste Sludge. *Int. J. Hydrogen Energy* **2017**, *42*, 9619–9629. [[CrossRef](#)]
32. Kamjunke, N.; Hertkorn, N.; Harir, M.; Schmitt-kopplin, P.; Griebler, C.; Brauns, M.; Von Tümpling, W.; Weitere, M.; Herzsprung, P. Molecular Change of Dissolved Organic Matter and Patterns of Bacterial Activity in a Stream along a Land-Use Gradient. *Water Res.* **2019**, *164*, 114919. [[CrossRef](#)] [[PubMed](#)]
33. Kamjunke, N.; Herzsprung, P.; Neu, T.R. Quality of dissolved organic matter affects planktonic but not biofilm bacterial production in streams. *Sci. Total Environ.* **2015**, *506–507*, 353–360. [[CrossRef](#)] [[PubMed](#)]
34. Zhou, Y.; Zhou, L.; Zhang, Y.; Garcia, J.; Souza, D.; Podgorski, D.C.; Spencer, R.G.M.; Jeppesen, E.; Davidson, T.A. Autochthonous Dissolved Organic Matter Potentially Fuels Methane Ebullition from Experimental Lakes. *Water Res.* **2019**, *166*, 115048. [[CrossRef](#)] [[PubMed](#)]



35. Huguet, A.; Vacher, L.; Relexans, S.; Saubusse, S.; Froidefond, J.M.; Parlanti, E. Properties of Fluorescent Dissolved Organic Matter in the Gironde Estuary. *Org. Geochem.* **2009**, *40*, 706–719. [[CrossRef](#)]
36. Shatilla, N.J.; Carey, S.K. Assessing Inter-Annual and Seasonal Patterns of DOC and DOM Quality across a Complex Alpine Watershed Underlain by Discontinuous Permafrost in Yukon, Canada. *Hydrol. Earth Syst. Sci.* **2019**, *23*, 3571–3591. [[CrossRef](#)]
37. Deshpande, B.N.; Maps, F.; Matveev, A.; Vincent, W.F. Oxygen Depletion in Subarctic Peatland Thaw Lakes. *Arct. Sci.* **2017**, *3*, 406–428. [[CrossRef](#)]
38. Pedersen, J.A.; Simpson, M.A.; Bockheim, J.G.; Kumar, K. Characterization of Soil Organic Carbon in Drained Thaw-Lake Basins of Arctic Alaska Using NMR and FTIR Photoacoustic Spectroscopy. *Org. Geochem.* **2011**, *42*, 947–954. [[CrossRef](#)]
39. Daoud, A.B.A.; Tremblay, L. HPLC-SEC-FTIR Characterization of the Dissolved Organic Matter Produced by the Microbial Carbon Pump. *Mar. Chem.* **2019**, *215*, 103668. [[CrossRef](#)]
40. Santos, E.B.H.; Duarte, A.C. The Influence of Pulp and Paper Mill Effluents on the Composition of the Humic Fraction of Aquatic Organic Matter. *Water Res.* **1998**, *32*, 597–608. [[CrossRef](#)]
41. Rodríguez, F.J.; Núñez, L.A. Characterization of Aquatic Humic Substances. *Water Environ. J.* **2011**, *25*, 163–170. [[CrossRef](#)]
42. Santos, E.B.H.; Duarte, R.M.B.O.; Filipe, O.S.; Duarte, A.C. Structural Characterisation of the Coloured Organic Matter from an Eucalyptus Pleached Kraft Pulp Mill Effluent. *Int. J. Environ. Anal. Chem.* **2000**, *78*, 333–342. [[CrossRef](#)]
43. Duarte, R.M.B.O.; Santos, E.B.H.; Duarte, A.C. Spectroscopic Characteristics of Ultrafiltration Fractions of Fulvic and Humic Acids Isolated from an Eucalyptus Bleached Kraft Pulp Mill Effluent. *Water Res.* **2003**, *37*, 4073–4080. [[CrossRef](#)]
44. Lopes, S.P.; Matos, J.T.V.; Silva, A.M.S.; Duarte, A.C.; Duarte, R.M.B.O. <sup>1</sup>H NMR Studies of Water- and Alkaline-Soluble Organic Matter from Fine Urban Atmospheric Aerosols. *Atmos. Environ.* **2015**, *119*, 374–380. [[CrossRef](#)]
45. Duarte, R.M.B.O.; Matos, J.T.V.; Paula, A.S.; Lopes, S.P.; Pereira, G.; Vasconcellos, P.; Gioda, A.; Carreira, R.; Silva, A.M.S.; Duarte, A.C.; et al. Structural Signatures of Water-Soluble Organic Aerosols in Contrasting Environments in South America and Western Europe. *Environ. Pollut.* **2017**, *227*, 513–525. [[CrossRef](#)] [[PubMed](#)]
46. Duarte, R.M.B.O.; Duarte, A.C. NMR Studies of Organic Aerosols. In *NMR Studies of Organic Aerosols. Annual Reports on NMR Spectroscopy*, 1st ed.; Webb, G.A., Ed.; Elsevier: London, UK, 2017; Volume 92, pp. 83–135. [[CrossRef](#)]
47. Einsiedl, F.; Hertkorn, N.; Wolf, M.; Frommberger, M.; Schmitt-kopplin, P.; Koch, B.P. Rapid Biotic Molecular Transformation of Fulvic Acids in a Karst Aquifer. *Geochim. Cosmochim. Acta* **2007**, *71*, 5474–5482. [[CrossRef](#)]
48. Woods, G.C.; Simpson, M.J.; Simpson, A.J. Oxidized Sterols as a Significant Component of Dissolved Organic Matter: Evidence from 2D HPLC in Combination with 2D and 3D NMR Spectroscopy. *Water Res.* **2012**, *46*, 3398–3408. [[CrossRef](#)] [[PubMed](#)]
49. Majumdar, R.D.; Bliumkin, L.; Lane, D.; Soong, R.; Simpson, J.; Simpson, M. Analysis of DOM Phototransformation Using a Looped NMR System Integrated with a Sunlight Simulator. *Water Res.* **2017**, *120*, 64–76. [[CrossRef](#)]
50. Duarte, R.M.B.O.; Silva, A.M.S.; Duarte, A.C. Two-Dimensional NMR Studies of Water-Soluble Organic Matter in Atmospheric Aerosols. *Environ. Sci. Technol.* **2008**, *42*, 8224–8230. [[CrossRef](#)]
51. Duarte, R.M.B.O.; Piñeiro-Iglesias, M.; López-Mahía, P.; Muniategui-Lorenzo, S.; Moreda-Piñeiro, J.; Silva, A.M.S.; Duarte, A.C. Comparative Study of Atmospheric Water-Soluble Organic Aerosols Composition in Contrasting Suburban Environments in the Iberian Peninsula Coast. *Sci. Total Environ.* **2019**, *648*, 430–441. [[CrossRef](#)]
52. Matos, J.T.V.; Duarte, R.M.B.O.; Lopes, S.P.; Silva, A.M.S.; Duarte, A.C. Persistence of Urban Organic Aerosols Composition: Decoding Their Structural Complexity and Seasonal Variability. *Environ. Pollut.* **2017**, *231*, 281–290. [[CrossRef](#)]
53. Simpson, A. Multidimensional Solution State NMR of Humic Substances: A Practical Guide and Review. *Soil Sci.* **2001**, *166*, 795–809. [[CrossRef](#)]

54. Hertkorn, N.; Permin, A.; Perminova, I.; Kovalevskii, D.; Yudov, M.; Petrosyan, V.; Kettrup, A. Comparative Analysis of Partial Structures of a Peat Humic and Fulvic Acid Using One- and Two-Dimensional Nuclear Magnetic Resonance Spectroscopy. *J. Environ. Qual.* **2002**, *31*, 375–387. [[CrossRef](#)] [[PubMed](#)]
55. Simpson, A.J.; Song, G.; Smith, E.; Novotny, E.H.; Hayes, M.H.B. Unraveling the Structural Components of Soil Humic by Use of Solution-State Nuclear Magnetic Resonance Spectroscopy. *Environ. Sci. Technol.* **2007**, *41*, 876–883. [[CrossRef](#)] [[PubMed](#)]
56. Zhang, F.; Harir, M.; Moritz, F.; Zhang, J.; Witting, M.; Wu, Y.; Schmitt-kopplin, P.; Fekete, A.; Gaspar, A.; Hertkorn, N. Molecular and Structural Characterization of Dissolved Organic Matter during and Post Cyanobacterial Bloom in Taihu by Combination of NMR Spectroscopy and FTICR Mass Spectrometry. *Water Res.* **2014**, *57*, 280–294. [[CrossRef](#)]
57. Hertkorn, N.; Harir, M.; Koch, B.P.; Michalke, B. High-Field NMR Spectroscopy and FTICR Mass Spectrometry: Powerful Discovery Tools for the Molecular Level Characterization of Marine Dissolved Organic Matter. *Biogeosciences* **2013**, *10*, 1583–1624. [[CrossRef](#)]
58. Duarte, R.M.B.O.; Santos, E.B.H.; Pio, C.A.; Duarte, A.C. Comparison of Structural Features of Water-Soluble Organic Matter from Atmospheric Aerosols with Those of Aquatic Humic Substances. *Atmos. Environ.* **2007**, *41*, 8100–8113. [[CrossRef](#)]
59. Cory, R.M.; McKnight, D.M.; Chin, Y.P.; Miller, P.; Jaros, C.L. Chemical Characteristics of Fulvic Acids from Arctic Surface Waters: Microbial Contributions and Photochemical Transformations. *J. Geophys. Res. Biogeosci.* **2007**, *112*, 1–14. [[CrossRef](#)]

**Publisher’s Note:** MDPI stays neutral with regard to jurisdictional claims in published maps and institutional affiliations.



© 2020 by the authors. Licensee MDPI, Basel, Switzerland. This article is an open access article distributed under the terms and conditions of the Creative Commons Attribution (CC BY) license (<http://creativecommons.org/licenses/by/4.0/>).